

See discussions, stats, and author profiles for this publication at: <https://www.researchgate.net/publication/265050788>

ATP Binding and Aspartate Protonation Enhance Photoinduced Electron Transfer in Plant Cryptochrome

ARTICLE in JOURNAL OF THE AMERICAN CHEMICAL SOCIETY · AUGUST 2014

Impact Factor: 12.11 · DOI: 10.1021/ja506084f

CITATIONS

11

READS

34

4 AUTHORS:



Fabien Cailliez

Université Paris-Sud 11

22 PUBLICATIONS 364 CITATIONS

[SEE PROFILE](#)



Pavel Müller

Atomic Energy and Alternative Energies Com...

26 PUBLICATIONS 433 CITATIONS

[SEE PROFILE](#)



Michaël Gallois

Université Paris-Sud 11

1 PUBLICATION 11 CITATIONS

[SEE PROFILE](#)



Aurélien de la Lande

Université Paris-Sud 11

38 PUBLICATIONS 448 CITATIONS

[SEE PROFILE](#)

ATP Binding and Aspartate Protonation Enhance Photoinduced Electron Transfer in Plant Cryptochrome

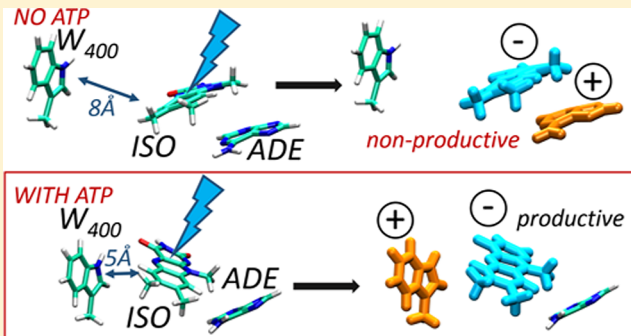
Fabien Cailliez*,† Pavel Müller,‡ Michaël Gallois,† and Aurélien de la Lande*,†

†Laboratoire de Chimie Physique, UMR 8000, Université Paris-Sud and CNRS, Orsay F-91405, France

‡UMR-8221, CEA-Institut de Biologie et de Technologies de Saclay, CNRS, Université Paris-Sud, Gif-sur-Yvette F-91191, France

Supporting Information

ABSTRACT: Cryptochromes are flavoproteins encountered in most vegetal and animal species. They play a role of blue-light receptors in plants and in invertebrates. The putative resting state of the FAD cofactor in these proteins is its fully oxidized form, FAD_{ox} . Upon blue-light excitation, the isoalloxazine ring (ISO) may undergo an ultrafast reduction by a nearby tryptophan residue W400. This primary reduction triggers a cascade of electron and proton transfers, ultimately leading to the formation of the FADH^{\bullet} radical. A recent experimental study has shown that the yield of FADH^{\bullet} formation in *Arabidopsis* cryptochrome can be strongly modulated by ATP binding and by pH, affecting the protonation state of D396 (proton donor to $\text{FAD}^{\bullet-}$). Here we provide a detailed molecular analysis of these effects by means of combined classical molecular dynamics simulations and time-dependent density functional theory calculations. When ATP is present and D396 protonated, FAD remains in close contact with W400, thereby enhancing electron transfer (ET) from W400 to ISO*. In contrast, deprotonation of D396 and absence of ATP introduce flexibility to the photoactive site prior to FAD excitation, with the consequence of increased ISO-W400 distance and diminished tunneling rate by almost two orders of magnitude. We show that under these conditions, ET from the adenine moiety of FAD becomes a competitive relaxation pathway. Overall, our data suggest that the observed effects of ATP and pH on the FAD photoreduction find their roots in the earliest stage of the photoreduction process; i.e., ATP binding and the protonation state of D396 determine the preferred pathway of ISO* relaxation.



INTRODUCTION

Cryptochromes are blue-light photoreceptors that are found in many living organisms, ranging from plants to animals and humans.^{1–3} They are involved in circadian rhythms⁴ and are suspected to play a role in the magnetoreception system of migratory birds.^{5–8} Cryptochromes are highly homologous to DNA-photolyases, although they lost the ability to repair DNA damage (with the exception of CRY-DASH cryptochromes that possess a single-stranded DNA-specific photolyase activity⁹). The structure of cryptochromes consists of two domains: the N-terminal domain (also called PHR: the photolyase homology region) and the flexible C-terminal domain. Crystallographic structures of the PHR domain structure exist for *Arabidopsis thaliana*,¹⁰ mouse,^{11,12} and *Drosophila*.^{11,13} The C-terminal of *Drosophila* cryptochrome has been resolved recently.^{11,13} In plant cryptochromes, the C-terminal tail is much longer, bulkier and intrinsically unstructured (unless it interacts with the PHR domain, in which case it may acquire a stable tertiary structure¹⁴).

Cryptochromes and photolyases bind flavin adenine dinucleotide (FAD) cofactor. Upon absorption of a blue photon, a fast intraprotein electron transfer (ET) can occur. This ET takes place between FAD (in a semireduced form FADH^{\bullet} in photolyases or in a fully oxidized form FAD_{ox} in cryptochromes)

and a chain of three tryptophan residues (labeled W400, W377, and W324 in *Arabidopsis thaliana* cryptochrome 1) that are conserved in the whole superfamily of photolyases and cryptochromes.^{15–18} The ET along the tryptophan triad has been extensively studied in photolyases, experimentally (see Brettel and Byrdin for a review¹⁶) as well as theoretically,^{18–21} and the mechanism and kinetics of this process is now well established. On the other hand, the situation is still unclear for cryptochromes. Despite numerous studies,^{17,18,22–29} many fundamental questions still remain open.

In 2003, Bouly et al. noticed that plant and human cryptochromes are able to bind ATP.³⁰ The crystallographic structure of *Arabidopsis thaliana* cryptochrome 1 (hereafter referred to as AtCRY1) reveals a plausible location for the binding of the ATP molecule to cryptochrome (Figure 1).¹⁰ In this structure, a molecule of adenosine 5'-(β,γ -imido)-triphosphate (AMP-PNP), a nonhydrolyzable analogue of ATP, was found to bind to the site corresponding to that of the pyrimidine-dimer binding in photolyases. More recently, it was shown that ATP binding to plant CRYs increases the amount

Received: June 17, 2014

Published: August 26, 2014

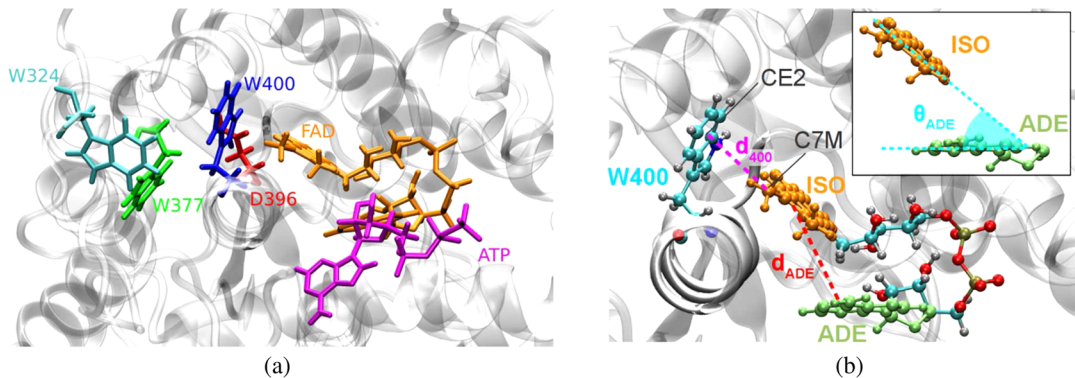


Figure 1. (a) Close-up view of the AtCRY1 reaction-center. FAD (orange), ATP (magenta), W400 (dark blue), W377 (green), W324 (cyan) and D396 (red) are highlighted in stick representation. (b) Geometrical parameters used to describe the structure of the active center during the simulations.

of FADH° accumulated upon photoreduction by slowing down the reoxidation process.^{24,31} The yield of FADH° formation increases from $\sim 2\%$ in the absence of ATP³² up to $\sim 15\%$ when ATP is present.³³ A conformational change induced by the presence of ATP was suggested by the authors as one of the possible causes of this phenomenon. Such a remarkable effect is likely to be biologically relevant. Müller et al. explored the link existing between ATP binding and electron- and proton-transfer kinetics in plant cryptochrome using time-resolved spectroscopy.³³ They showed that the presence of ATP not only dramatically increases the yield of the light-induced transients but also alters the kinetics of their formation and their decay in AtCRY1. These results are indicative of a change in the photoreduction mechanism. The yield of FADH° production was also shown to be enhanced by lowering the pH (in the absence of ATP). Since both ATP binding and lowering the pH had also a very similar effect on the UV-vis spectrum of FAD_{ox} the authors suggested that the presence of ATP, among other things, modulates the pK_a of the aspartic acid D396, the amino acid, which is most likely to protonate the photoinduced FAD° . Among theoreticians, ATP-binding has not been given much attention so far. Exner et al. performed molecular dynamics (MD) simulations on *Arabidopsis thaliana* cryptochrome 1 (AtCRY1) with and without ATP.³⁴ They concluded that ATP-binding reduces the flexibility of a few small segments of cryptochrome, located in the vicinity of the ATP binding site. However, they did not comment on the possible impact of ATP-binding on the electron transfer in cryptochrome.

The results of Müller and co-workers are connected to another yet unresolved question about the mechanism of ET in AtCRY1. Photoreduction of FAD_{ox} yields semireduced FADH° radical. On the basis of time-resolved absorption studies on algal *Chlamydomonas* photolyase homologue 1, Langenbacher et al. estimated that ET in the whole tryptophan chain takes place within few hundreds of picoseconds,²⁵ followed by deprotonation of the terminal tryptophan ($\text{W324}(\text{H})^{+}$) in less than 200 ns and protonation of the semireduced flavin within $\sim 1.7 \mu\text{s}$.²² On the contrary, on the basis of computer simulations, Solov'yov et al. proposed an ultrafast proton transfer following the first ET from the first tryptophan of the triad (W400) to FAD_{ox}^* and prior to the hole transfer along the tryptophan triad.²⁸ Müller et al.³³ proposed recently that the two mechanisms may coexist and the protonation is either ultrafast, yielding a pair of neutral radicals $\text{FADH}^\circ-\text{W400}^\circ$ next to a neutral (protonated) D396(H), or takes place on the microsecond time scale, yielding the products of the hole transfer through the tryptophan triad:

$\text{FADH}^\circ-\text{W324}^\circ$ and an anionic D396⁻, which, they suggest, could be a trigger of a larger conformational change leading to transduction of the light signal to cryptochrome partners. The latter mechanism is preferred under all circumstances but the proportion of the ultrafast proton transfer mechanism was found to be significant in the absence of ATP.³³

After excitation by blue or near-UV light, the oxidized FAD cofactor may relax along multiple channels, but only some of them eventually lead to the formation of one of the possible $\text{FADH}^\circ-\text{Trp}^\circ$ radical pairs. It is noteworthy that the yield for the formation of these pairs is far below 1, which may reflect either a strong competition between the productive ET and other ISO* de-excitation pathways, or a fast recombination of the $\text{FAD}^\circ-\text{W400}(\text{H})^{+}$ pair. Experimental data of Müller et al. showed that ATP binding considerably enhances the yield of FADH° production. On the other hand, since the ATP binding site is located on the opposite side of FAD than the tryptophan triad, ATP is not likely to have a major effect on the hole transfer through the triad. Instead, it could influence already the branching among the individual FAD^* relaxation pathways.

The major competitive relaxation channels (with respect to ET from W400) that might, in principle, be considered in the first picoseconds after FAD excitation are (i) interconversions among the manifold of singlet states (ii) intersystem crossing between the singlet and triplet states, (iii) fluorescence and (iv) competitive ET to ISO* from electron donors other than W400. Internal conversions between the flavin singlet excited states are likely to take place on the subpicosecond time scale and are therefore probable competitive channels for the $\text{W400} \rightarrow \text{ISO}^*$ ET. However, they are likely to be governed by local dynamics on the isoalloxazine moiety and probably do not depend so much on the local environment of flavin (protonation of D396 or ATP-binding). The characteristic time of intersystem crossing to the triplet state is on the order of a few ns, as observed for flavin in solution or in protein like LOV receptors or in BLUF domains³⁵⁻³⁷ and should not be able to compete with ET from W400. Quantum yield of fluorescence of free FAD is $\sim 5\%$ and even lower (or even completely missing) if FAD is protein-bound,³⁸ fluorescence can therefore hardly be considered as an important deactivation pathway. Regarding other electron donors in the vicinity of FAD that could quench electron transfer from W400, one may think of the adenine moiety (ADE) of flavin that, due to the particular U-shape of flavin, is located near the isoalloxazine moiety. Interestingly, Liu et al. have investigated the kinetics of such electron transfer in photolyases and found that ADE \rightarrow ISO* takes place within 19 ps (in the case

of initially oxidized flavin like in cryptochromes).²⁶ ET from other donors such as tyrosine Y402 (6 Å from ISO) or adenine of ATP (when present) are also plausible. In summary, some pathways may compete with the formation of the biologically relevant FAD^{o-}–W400(H)^{o+} pair in *AtCRY1*. The working hypothesis of the present study is that ATP binding enhances the rate of the initial W400 → ISO* ET step, making it more competitive with alternative deexcitation pathways. Given the experimental data of Müller et al., this effect may also be correlated to the protonation state of D396. In this paper, we use computational methods to explore the impact of ATP binding and of protonation of D396 on the first ET step in *AtCRY1-PHR*. The objectives of the present study are thus: (i) to investigate the dynamics of *AtCRY1* photoactive site in absence and presence of ATP for the two protonation states of D396, (ii) to compare the probability of W400 → ISO* ET with that from ADE → ISO* for the four possible systems: D0, DA, P0, PA, where “D” stands for deprotonated D396, “P” for protonated D396, ‘0’ indicates the absence of ATP and “A” its presence.

We first present the Computational Methods used in this study. In the Results section, we show how protonation of D396 and ATP binding enhances the electron transfer between W400 and ISO* thanks to the stabilization of the photoactive site. We then investigate the kinetics of the competitive intraflavin electron transfer between the adenine and isoalloxazine moieties of FAD. We show that this alternative route should become important when D396 is deprotonated. The theoretical results are compared to experimental observations in the Discussion section.

COMPUTATIONAL METHODS

Molecular Dynamics Simulations of *AtCRY1-PHR*. Classical molecular dynamics (MD) simulations have been performed to sample the structure and dynamics of *AtCRY1* depending on the protonation state of D396 and the binding of ATP. The four systems studied are listed in Table 1.

Table 1. List of the 4 Systems Studied in This Work and the Lengths of the 5 Simulations Performed for Each System

name	protonation state of D396	ATP binding	md1 (ns)	md2 (ns)	md3 (ns)	md4 (ns)	md5 (ns)
D0	deprotonated	no	150	50	25	25	25
DA	deprotonated	yes	150	50	25	25	25
P0	protonated	no	150	50	25	25	25
PA	protonated	yes	150	70	25	25	25

The *AtCRY1-PHR* starting structure has been taken from the 1U3D structure¹⁰ of the Protein Data Bank (PDB).³⁹ In this structure, an ATP-analogue (AMP-PNP) is bound in lieu of ATP. Since this structure is virtually identical to the ATP-free structure also available in the PDB (1U3C), we chose to use only 1U3D structure as a template for all four systems studied here (D0, DA, P0, and PA). All crystallographic water molecules were kept, as well as magnesium and chloride ions that are present both in 1U3C and 1U3D structures. In the latter, another magnesium ion is found in the vicinity of the AMP-PNP and is thus included in the simulations of systems PA and DA. The ATP molecule is constructed by substituting N3B atom of AMP-PNP by an oxygen atom. A molecule of 3-[ethyl(dimethyl)ammonio]propane-1-sulfonate cocrystallized with *AtCRY1-PHR* has been removed. Default protonation states were used for all titratable residues except D396. All the systems were immersed in a 105 Å-edged cubic TIP3P⁴⁰ water box. Sodium and chloride ions were added to achieve a salt concentration of approximately 0.05 M.

We used CHARMM27 force field with CMAP corrections⁴¹ to describe cryptochrome and ATP molecules. A force field for oxidized flavin FAD molecule was developed for this study (see details in Supporting Information). Molecular dynamics simulations on the ground electronic state of the flavin have been performed using NAMD2.8.⁴² Periodic boundary conditions are used in all simulations. Electrostatic interactions are computed using the Particle Mesh Ewald summation. Lennard-Jones and electrostatic potentials are truncated at a cutoff of 12 Å, using a switching function. Shake algorithm⁴³ is used to constrain bonds including hydrogen atoms and a time step of 2 fs is used. Simulations are performed in the isothermal-isobaric NPT ensemble at 300 K and under a pressure of 1 atm. Temperature is controlled by applying Langevin forces with a damping coefficient of 1 ps⁻¹. The pressure is controlled using a Nosé-Hoover Langevin piston.^{44,45} Each system was first submitted to a 10 000-steps energy minimization of the solvent, then heated from 100 to 300 K in 200 ps, with 10 kcal mol⁻¹ positional restraints on solute heavy atoms. Finally, restraints were gradually decreased in the course of 800 ps of NPT molecular dynamics. Five different schedules were used to release the restraints, leading to five different initial conditions for molecular dynamics. After equilibration, production runs were performed for at least 25 ns. The lengths of all the simulations performed in this work are given in Table 1.

Evaluation of pK_a Shifts. We have estimated the shift in pK_a of D396 due to ATP binding using continuum electrostatics calculations (CEC) based on the Poisson-Boltzmann (PB) equations. It is known that pK_a computations using CEC suffer from limitations, especially when significant conformational change arises upon (de)protonation.⁴⁶ Thus, the values obtained with such methods cannot be expected to match experimental data quantitatively. Nevertheless, they should provide a qualitative indication of the change in D396 pK_a associated with ATP binding.

The PBEQ module of CHARMM⁴⁷ has been used to solve the PB equations. This is achieved in two successive steps using first a coarse-grid (approximately 1.3 Å mesh size) and then a second finer grid (0.25 Å mesh size) focused on D396. We employed a set of atomic Born radii, optimized by Roux and co-workers to reproduce free energies of solvation of amino and nucleic acids.⁴⁸ Dielectric constants of 4 and 80 have been set for protein and water, respectively. pK_a shifts with respect to pK_a of an aspartic acid in water have been computed on protein structures (including flavin and ATP cofactors when present but removing all ions and water molecules) extracted from MD simulations every 500 ps.

Photoinduced Electron Transfer Rates. From a theoretical point of view, the rate of electron transfer between a donor (D) and an acceptor (A) depends on the fluctuations of the energy gaps between the relevant electronic states and on the coupling terms between them. Typically, one uses a two-states diabatic picture to describe electron transfer between D and A, in which the first electronic state {D,A} represents the situation before charge transfer and the second electronic state {D⁺,A⁻} is the situation where the charge transfer has taken place. Charge transfer kinetics between D and A is determined on one hand by the probability to achieve molecular configurations for which the potential energies of the two states are degenerated (activated configurations)⁴⁹ and on the other hand by the probability of population exchanges between degenerated electronic states. The latter is primarily determined by the strength of the coupling.

Computational modeling of ultrafast ET may be achieved through different methodologies. One may choose to carry out non-Born-Oppenheimer (BO) MD simulations based for example on the Tully's surface hopping⁵⁰ or Mean-Field schemes.⁵¹ The objective of these semiclassical approaches is to simulate the time evolution of the electronic wave function, including population exchanges between {D,A} and {D⁺,A⁻}. Quantum chemistry computations are carried out on-the-fly along the MD simulation to calculate the forces acting on the nuclei and to propagate the time-dependent Schrödinger equation for the electronic wave function. Meaningful results are obtained after averaging over large ensembles of reactive non-BO trajectories. As an illustration, we mention the studies of Elstner and co-workers who conducted Ehrenfest MD simulations for charge migration in DNA⁵² or along the tryptophan triad of DNA photolyases.²⁰ These authors

employed a self-consistent-charge tight binding density functional theory methodology to reduce the computational cost of the simulations. Non-BO MD simulations are well adapted if one is interested in the processes by which population exchanges are taking place.

Alternatively, one may rely on macroscopic kinetic models like the Marcus theory. These models provide expressions for calculating ET rates as a function of macroscopic variables like the activation free energy or the reorganization energy. A common computational strategy will thus involve providing estimates of these quantities using microscopic simulations. This computational strategy has been reviewed on several occasions and can now be seen as well established. In the Marcus theory framework, the rate of electron transfer k^{ET} is given by

$$k^{\text{ET}} = \frac{2\pi}{\hbar} \frac{1}{\sqrt{4\pi\lambda k_B T}} |H_{12}|^2 \exp\left(-\frac{\Delta G^\ddagger}{k_B T}\right) \quad (1)$$

where T is the temperature, k_B and \hbar are the Boltzmann and the reduced Planck constant, respectively, λ is the reorganization energy, ΔG^\ddagger is the activation free energy, and H_{12} is the electronic coupling between the states $\{\text{D},\text{A}\}$ and $\{\text{D}^+,\text{A}^-\}$. Some of the underlying hypotheses of the Marcus theory, like the linear response approximation or the instantaneous thermodynamic relaxation of the environment, may not be entirely fulfilled for an ultrafast ET. However, this framework provides insightful elements for comparing how fast electron transfer proceeds in molecular systems with a high degree of similarity, as will be the case here when comparing ET rates between the D0, DA, P0, and PA systems. For instance, Parson and Warshel investigated the initial electron-transfer step between the so-called special pair and the bacteriopheophytin pigment in the photosynthetic reaction center of the bacteria *Rhodopseudomonas viridis* in various environments within the Marcus theory framework.⁵³

In addition to the hypotheses of the Marcus theory, we propagated MD simulations on the ground state potential energy surface (PES), instead of the one of the excited state. Because the ET process occurs immediately after the flavin excitation (ps time scale), little reorganization of the environment is expected to take place prior to this ET, so that the configurations sampled from the ground state MD simulations are thought to be suitable for investigating ultrafast ET from the excited state. On the other hand, the ISO ring itself is likely to have time to relax on the excited surface before the first ET step takes place. Some non-equilibrium contributions (NECs) may thus enter the actual ET rate, although these will not be taken into account in our theoretical estimates based on the Marcus theory and on the realization of MD simulations on the ground state PES. Nevertheless, the changes in geometry between the ground and first excited states are limited to a few bonds of the ISO ring (Figure S4). Furthermore, the variations of the bond lengths between those two states are similar in magnitude to their fluctuations during MD simulations (standard deviations of the bond lengths are of the order of 0.03 Å). We thus may anticipate that NECs will be moderate. Finally, the errors in ET rate estimations due to such NECs are expected to be systematic for the D0, DA, P0, and PA systems and therefore should not hamper a meaningful qualitative comparison of these rates.

Energetics of Charge Transfer Processes. The important excited states involved in photoreduction of AtCRY1 are (i) those associated with the $\pi \rightarrow \pi^*$ transitions (S1 and S3) and with dark $n \rightarrow \pi^*$ transition (S2) of the oxidized ISO, (ii) the one associated with the charge transfer state from W400 or ADE to ISO. Experimentally, the initial excitation commonly target the S1 state, but excitation in S3 is also possible. Note that internal conversions among the manifold of singlet π^* states are likely to take place on the 100 fs to 1 ps time scale. It is thus possible that some reactive ET pathways proceed via a preliminary S3 \rightarrow S1 or S3 \rightarrow S2 transition. Experiments do not show dependence on the excitation wavelength and we thus suppose that S1 is the ISO* electronic state involved in the CT process. Energies of the $\{\text{ISO}^*,\text{W400}\}$, $\{\text{ISO}^-, \text{W400}^+\}$ and $\{\text{ISO}^-, \text{ADE}^+\}$ electronic states were evaluated using time-dependent density functional theory (TD-DFT) calculations.⁵⁴ TD-DFT calculations were performed with the Gaussian09 software (version D.01).⁵⁵ All calculations were performed with the

TZVP basis set (triple-zeta with valence-polarization functions).⁵⁶ The list of atoms treated at the DFT level is comprised of the FAD isoalloxazine and adenine moieties and the D396 and W400 side chains. It represents a total of 86 atoms (85 when D396 is deprotonated). The valences of the carbon atoms were saturated when needed using the link atom technique.^{57,58} Electrostatic effects of the environment were taken into account by including the force field charges in the DFT calculations. Assignments of the electronic excitations were based on the localization of the occupied and of the virtual molecular orbitals associated with the main orbital transition. Thanks to the use of hybrid functional, the attribution process was straightforward (few mixing of valence and charge transfer transitions were observed, unlike when nonhybrid functionals are used).

It is well-known that CT processes are poorly described by most DFT functionals, especially those lacking non-local Hartree–Fock exchange.⁵⁹ The use of global hybrid or range-separated hybrid functionals alleviates this problem but sometimes at the price of degrading the quality of the description of local valence excitations. Various benchmark studies have been published in the recent past.^{60–62} In a preliminary phase, we performed a series of test calculations to find the most adequate functionals for the systems of our present interest (see Supporting Information). Our tests showed that range-separated functionals like CAM-B3LYP,⁶³ M11⁶⁴ or ω B97X-D⁶⁵ were required to deal with the fluctuations of CT energies as a function of the variations of the ISO–W400 distance. We selected ω B97X-D as a good compromise between the description of valence and charge transfer excitations. Importantly, we checked that the trends in characteristic ET rate variations between systems D0, DA, P0 and PA, on which our main conclusions are based, were not sensitive to a particular choice among the aforementioned range-separated functionals (see Supporting Information).

Electronic Coupling and Tunneling Pathways. The electronic coupling H_{12} between $\{\text{ISO}^*,\text{W400}\}$ and $\{\text{ISO}^-, \text{W400}^+\}$ electronic states has been estimated along the MD simulations using two complementary approaches: the generalized Mulliken–Hush method (GMH),⁶⁶ and the empirical pathway model (PM).^{67,68} The GMH scheme provides means to estimate the coupling based on the TD-DFT results:

$$H_{12} = \frac{\mu_{ab} \Delta E_{ab}}{\sqrt{\Delta\mu^2 + 4\mu_{ab}^2}} \quad (2)$$

μ_{ab} and ΔE_{ab} are the transition dipole moment and the energy gap between the adiabatic states a and b corresponding to the CT process, respectively. $\Delta\mu$ is the difference of permanent dipole moments of the two adiabatic states. The transition dipole moment between CT states and the excited S1 state was approximated by the transition dipole moments between CT and S0 state. This is justified by the fact that S0 \rightarrow S1 excitation is localized on the ISO ring. The permanent dipole moments of the $\{\text{ISO}^*,\text{W400}\}$ and $\{\text{ISO}^-, \text{W400}^+\}$ electronic states were estimated using MM force field charges. The GMH approach has two advantages. First, it provides a quantum mechanical estimate of H_{12} . Second, it is applicable to geometries that do not necessarily correspond to situations of degeneracy. On the other hand, it requires expensive TD-DFT calculations, and, as a consequence, has been applied to only a few hundreds of geometries for each system. The method was also applied to estimate the electronic coupling for the ADE \rightarrow ISO* ET.

The PM developed by Beratan and co-workers provides a complementary approach to rationalize the variations of H_{12} between the different systems at a much lesser computational cost.^{67,68} This model is built on the assumption that the electron tunnels from the electron donor (W400) to the acceptor (ISO*) along a pathway that is defined as a succession of covalent or hydrogen bonds and of through space (van der Waals) contacts. The decay of the electronic coupling associated with a given pathway is expressed as the product of multiplication of a constant contact coupling (H_{12}^{contact}) by a factor (ϵ_{tot}) that reflects the attenuation of the coupling caused by the presence of intervening medium between W400 and ISO. ϵ_{tot} depends on the number of covalent or hydrogen bonds (denoted N_c and N_{hb} , respectively) and of through-space jumps (N_{ts}) composing the electron

Table 2. TD-DFT (ω B97X-D functional) Results for the FAD Valence Transitions and for the W400 \rightarrow ISO* and ADE \rightarrow ISO* Charge Transfer States^a

	D0		DA		P0		PA	
	excitation energy (eV)	oscillator strength						
FAD S1 (exp. 2.79 eV)	2.97 \pm 0.14	0.184	2.99 \pm 0.14	0.185	2.96 \pm 0.15	0.196	2.95 \pm 0.13	0.195
FAD S2	3.46 \pm 0.31	0.011	3.47 \pm 0.30	0.012	3.42 \pm 0.29	0.010	3.41 \pm 0.30	0.011
FAD S3 (exp. 3.42 eV)	3.67 \pm 0.23	0.153	3.68 \pm 0.21	0.159	3.75 \pm 0.27	0.163	3.70 \pm 0.24	0.171
CT _{W400 \rightarrow ISO*}	3.79 \pm 0.40	0.001	3.69 \pm 0.40	0.001	3.66 \pm 0.41	0.002	3.45 \pm 0.34	0.006
CT _{ADE \rightarrow ISO*}	4.03 \pm 0.39	0.010	4.02 \pm 0.43	0.012	4.06 \pm 0.43	0.015	4.04 \pm 0.37	0.010

^aEach number corresponds to an average over around 550 TD-DFT calculations.

transfer pathway. This factor is calculated according to a set of mathematical expressions empirically calibrated by the authors of the model:

$$H_{12} = H_{12}^{\text{contact}} \epsilon_{\text{tot}} \quad (3)$$

$$\epsilon_{\text{tot}} = \prod_{N_c} \epsilon_c \times \prod_{N_{\text{hb}}} \epsilon_{\text{hb}} \times \prod_{N_{\text{ts}}} \epsilon_{\text{ts}} \quad (4)$$

$$\epsilon_c = 0.6 \quad (5)$$

$$\epsilon_{\text{hb}} = 0.36 \times \exp[-\beta_s(R_H - 2.8)] \quad (6)$$

$$\epsilon_{\text{ts}} = 0.6 \times \exp[-\beta_s(R_S - 1.4)] \quad (7)$$

In these equations, R_S is the atom–atom distance for through-space jumps, R_H is the hydrogen bond length (taking the interheavy atom distance) and β_s is a characteristic decay factor set to 1.7 Å⁻¹ in our computations. The nitrogen and carbon (except those of the methyl groups) atoms of the ISO ring, as well as the W400 side chain, were made conductive (i.e., $\epsilon_c = 1$ between two such atoms) in our analysis so that the PM results do not depend on the particular choice of the donor/acceptor atom within these rings. This choice is guided by the delocalization of the donor and acceptor molecular orbitals over the atoms holding the π -system. The best pathway was identified for each analyzed structure using the Dijkstra algorithm⁶⁹ with an in-house program.^{70,71} Structures were extracted from the MD simulations every 5 ps and analyzed with the PM. To make the pathway search tractable, the structure was preliminarily pruned to include only the atoms susceptible to taking part in the tunneling process. Besides its low computational cost, another remarkable property of the PM model is that it renders a visual picture of the tunneling event. Provided the PM is coupled to a methodology for sampling the dynamics of the intervening medium, it exhibits a remarkable efficiency in reproducing experimental ET rates, sometimes with quantitative accuracy (see for example ref 72.).

RESULTS

We investigated how ATP binding and/or protonation of D396 impacts the yield of FAD_{ox} reduction in AtCRY1-PHR. Our working hypothesis throughout this work was that the variation of this yield in the 4 systems is due to variations of the kinetics of the W400 \rightarrow ISO* electron transfer. To test this hypothesis, we completed hundreds of nanoseconds of classical molecular dynamics trajectory coupled to extensive quantum chemistry (TD-DFT) calculations (see the computational protocol for details) and estimated the rate of ET to ISO*. These extensive MD simulations are necessary to sample the ensemble of conformations that the protein is susceptible to adopt prior to FAD excitation. In the following, we present our results regarding the impact of ATP binding and/or protonation of D396 on the electron transfer from W400 to ISO*. We then show similar data for the competitive ADE \rightarrow ISO* electron transfer. The role of ATP binding on the modulation of D396 pK_a is finally described.

Electron Transfer from W400 to ISO*. Energetic Aspects.

TD-DFT computations were carried out on structures extracted from the MD simulations (Table 1) with a period of time of 500 ps. This led to ensembles of around 550 geometries for each of the four systems (D0, DA, P0 and PA). We remind that TD-DFT results take into account the polarization of the redox cofactors by the environment including protein residues and water molecules. Statistics of the TD-DFT calculations are presented in Table 2. Transitions from S0 to the excited states S1 and S3 can be ascribed to $\pi \rightarrow \pi^*$ transitions within the ISO rings. They correspond to the experimentally observed absorption bands at 2.79 and 3.42 eV. The theoretical values slightly overestimate the experimental ones by 0.2 to 0.3 eV. Variations of the average energies of S1 and S3 between the 4 systems are smaller than the fluctuations of the energy levels due to variations of the local structure of the redox cofactor or of the position of the surrounding atoms observed in one system. Thus, the computations do not predict significant shifts of the absorption bands when ATP is added to the medium and/or if D396 is deprotonated. The S2 excited state is associated with a weak oscillator strength for the S0 \rightarrow S2 transition which corresponds to a valence $n \rightarrow \pi^*$ transition. S2 may thus be involved in charge transfer processes, but only via preliminary interconversions from higher excited states like S3. Again, the energy position of the S2 excited state is not appreciably modified by (de)-protonation of D396 or ATP-binding.

Let us now examine the excited states associated with electron transfer from W400 to ISO*. On average, the CT_{W400 \rightarrow ISO*} state lies ca. 0.5 to 0.8 eV above the S1 state. We observe a small increase of the average energy level of the CT state when D396 is deprotonated. However, the physical significance of this trend has to be taken with caution. Indeed the fluctuations of the energy gap between the electronic states are more relevant for the ET rates than their mere average positions. In that regard, it is instructive to look at the fluctuations of the energy gap in the system PA shown in Figure 2a. In terms of energy, the S1 and CT_{W400 \rightarrow ISO*} states come often very close to each other; this is also illustrated by Figure 2b, which shows the probability distribution of the energy gap (ΔE) between the two states. The picture described here for the PA system is similar for the other 3 cases (see Figure S5 to S7), which means that the probability to reach a configuration of similar energy for the S1 and CT_{W400 \rightarrow ISO*} state just after the excitation is large and similar regardless of the protonation state of D396 or the presence of ATP in the binding pocket.

Electronic Coupling and Tunneling Pathways. The average values of the electronic coupling calculated with the GMH scheme are reported in Table 3. A strong variation of almost 1

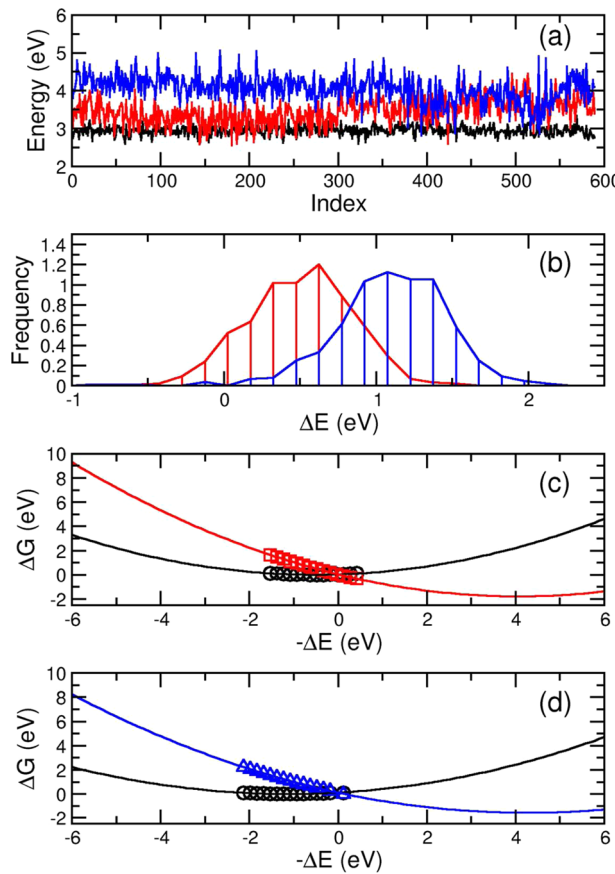


Figure 2. Energetics of electron transfer to flavin in PA system. (a) Energies of the S1 (black), $\text{CT}_{\text{W}400 \rightarrow \text{ISO}^*}$ (red), and $\text{CT}_{\text{ADE} \rightarrow \text{ISO}^*}$ (blue) states for structures extracted from the classical MD simulations. (b) Probability distribution of energetic gaps between $\text{CT}_{\text{W}400 \rightarrow \text{ISO}^*}$ and S1 states (red) and between $\text{CT}_{\text{ADE} \rightarrow \text{ISO}^*}$ and S1 states (blue). (c) Free energy curves for the S1 (black circles) and $\text{CT}_{\text{W}400 \rightarrow \text{ISO}^*}$ (red squares) electronic states obtained with LRA approximation (see Supporting Information for technical details), as a function of the energetic gaps between the two states. The lines are the results of a quadratic fit. (d) Same as (c) but for S1 (black circles) and $\text{CT}_{\text{ADE} \rightarrow \text{ISO}^*}$ (blue) states.

Table 3. Mean Unsigned Electronic Coupling (in cm^{-1}) Computed with the GMH Scheme from Approximately 550 TD-DFT ($\omega\text{B97X-D}$ Functional) Results^a

	D0	DA	P0	PA
$\text{W}400 \rightarrow \text{ISO}^*$	9 (23)	12 (28)	30 (52)	56 (76)
$\text{ADE} \rightarrow \text{ISO}^*$	183 (152)	169 (158)	133 (144)	99 (99)

^aThe numbers in brackets are the standard deviations.

order of magnitude is found between systems PA (56 cm^{-1}) and the deprotonated systems D0 (9 cm^{-1}) and DA (12 cm^{-1}). The mean electronic coupling in the system P0 is intermediate (30 cm^{-1}). Actually, as for the position of the energy levels, the most significant information can be extracted from the distribution of the H_{12} values.^{73,74}

Figure 3a shows the values of the electronic coupling for the PA system for sampled structures extracted from MD simulations. The fluctuations of H_{12} are very important, which is revealed by a standard deviation which is as large as the mean value (see Table 3). This finding is also true for P0, DA, and D0 systems. This means that fluctuations play a major role in controlling the kinetics of the electron transfer, which is likely to

be dominated by structures with electronic strong coupling values. Figure 3b depicts histograms of $|H_{12}|$ for the 4 systems. Note that the probability to have a large electronic coupling is much greater in protonated (P0 and PA) than in deprotonated systems, which will lead to a higher ET rate. Comparing P0 and PA, it can be concluded that electronic coupling values are slightly larger when ATP is bound to cryptochrome, but this effect is much less pronounced than that induced by D396 deprotonation.

The relative values of electronic couplings for the four systems correlate with structural changes within the photoactive center observed during the MD simulations. In particular, the distance between the donor W400 and the acceptor ISO* is found to become shorter from D0 through DA and P0 to PA. This is shown in Figure 4, where histograms of the distance d_{400} between the central carbon atom of the indole ring of W400 (CE2 in PDB nomenclature) and the C7M atom of ISO computed during the course of molecular dynamics simulations are drawn. A strong deviation from crystallographic structure is observed in deprotonated systems D0 and DA that leads to an increase of d_{400} and consequently to a decrease of the electronic coupling. Such structural deviation is also seen in P0 system for some of the MD simulations, but it has never been observed for PA. Protonation of D396 thus stabilizes the photoactive center in conformation, in which W400 and ISO are close to each other, enhancing the electronic coupling. The impact of ATP binding is less pronounced but it further reduces the distances between W400 and ISO.

The general evolution of H_{12} from one structure to another is roughly accounted for by the evolution of the distance between W400 and the ISO ring. To go one step further, we conducted an analysis of the electron tunneling pathways. The outcomes of the PM analysis are fully consistent with the GMH scheme (see Figure 3b). The resemblance of the two sets of histograms is remarkable, indicating that the PM is in qualitative agreement with the results provided by the GMH scheme and is adequate to describe the ET between W400 and ISO*. The PM analysis further validates the sample size chosen for the computation with the GMH scheme (one of the major advantages of the PM is that it allows analysis of much larger structure samples due to its low computational cost).

The tunneling pathway analysis leads to a deconvolution of the global decay factor distribution in terms of distinct contributions arising from pathways of different nature. We have classified the pathways observed in the simulation into four categories (Figure 5 and Table S5). The first category (labeled A) corresponds to pathways directly connecting the ISO ring to the W400 side chain (an example is depicted in Figure 5, left). Because pathways A involve a “through-space” jump, they dominate only when the distance between ISO and W400 is short. It is an exclusive pathway encountered along the MD simulations of system PA (>95%), and it remains dominant for P0 (ca. 70%). On the contrary, it is rarely observed for systems D0 and DA (<15%). This last point has to be seen as a consequence of the increase of the distances between the isoalloxazine ring and W400 (Figure 4): this distance becomes so large in D0 and DA that type A pathways are inefficient in mediating electron tunneling. In systems D0, DA, and P0, a new type of pathway (labeled B) appears. It corresponds to a pathway running through D396. In P0, this pathway may be “open” when a hydrogen bond is formed between D396 and ISO-O4 (see Figure 5 for an example of such pathway). The formation of this hydrogen bond requires the breaking of the hydrogen bond between D396 side chain and the

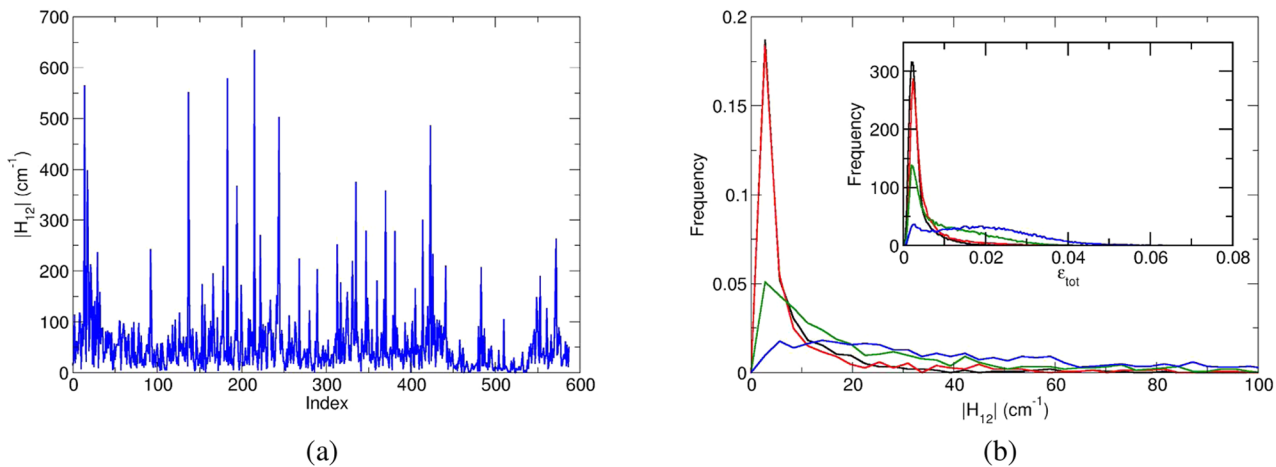


Figure 3. Electronic coupling between S1 and $\text{CT}_{\text{W}400 \rightarrow \text{ISO}^*}$ states. (a) Fluctuation of the absolute value of the electronic coupling in the PA system, computed with the GMH scheme over structures sampled from the MD simulations. (b) Histograms of $|\mathcal{H}_{12}|$ in cases D0 (black), DA (red), P0 (green), and PA (blue). The inset graph shows histograms of the decay factor ε_{tot} from PM analysis. Color code is the same in both graphs.

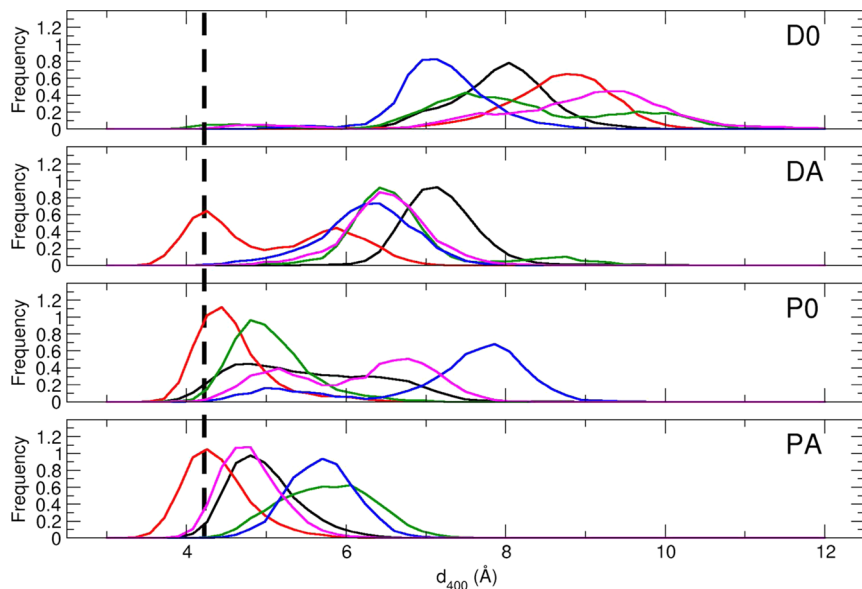


Figure 4. Normalized distributions of the distance d_{400} between W400 and ISO during MD simulations. The dashed black line is the value of d_{400} in the crystallographic structure. Each panel represents one molecular system and each colored histogram stands for one MD simulation (black: md1, red: md2, green: md3, blue: md4, magenta: md5).

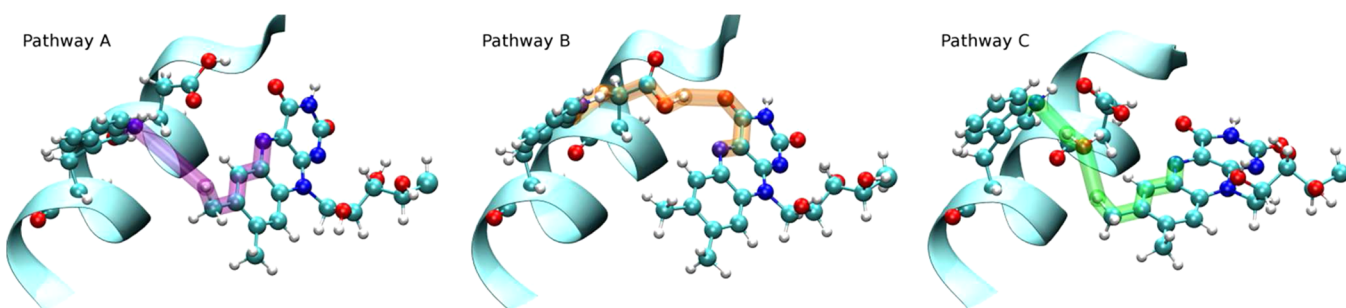


Figure 5. Schematic view of the main characteristic electron transfer pathways. The pathways are represented as transparent tubes. For clarity, only W400, D396, and the isoalloxazine group are displayed in ball and stick representation, as well as any other residue directly involved in the pathway. The helix bearing W400 is also represented in schematic representation. Left image: pathways of category A connecting directly W400 and ISO (purple). Middle image: pathways of category B involving D396 as a bridge (orange). Right image: pathway of category C involving a water molecule (green).

carbonyl group of methionine M381 which is found in the crystallographic structure. Such configurations are frequently observed in P0 system (almost 70% of simulation time), whereas

they are almost never seen in PA simulations (see Figure 6). In D0 and DA systems, no direct hydrogen bond can be formed between D396 and ISO, but in many cases, one or two

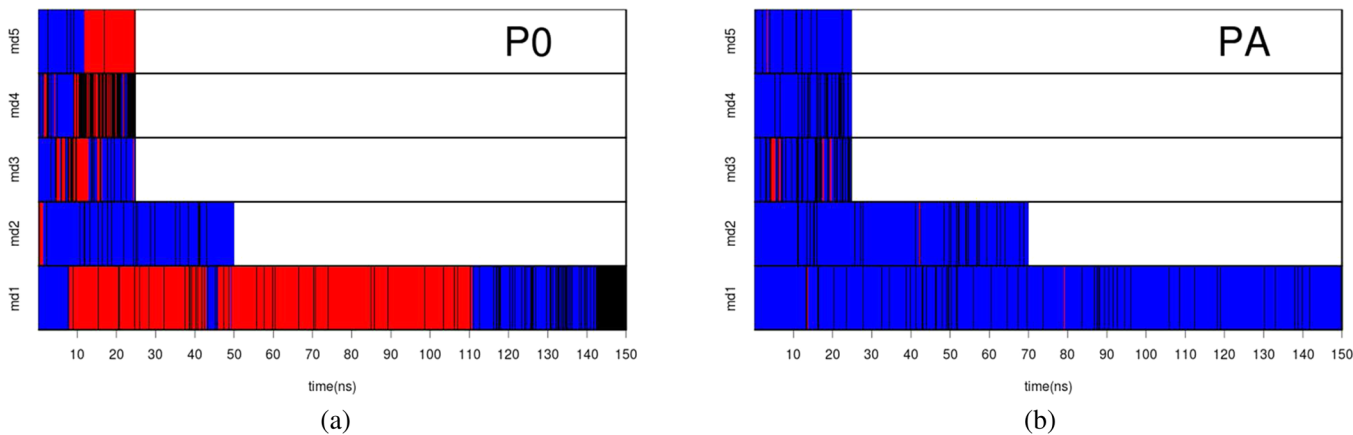


Figure 6. H-bonds made by the carboxylic group of D396 when protonated in systems (a) without ATP or (b) with ATP. Blue: H-bond formed with M381, red: H-bond formed with ISO-O4, black: no H-bond. Each horizontal bar in each plot represents a single simulation.

Table 4. Estimation of ET Rates from Marcus Theory for W400 → ISO* ET^a

system	activation free energy ΔG^\ddagger (eV)	reorganization energy λ (eV)	mean squared electronic coupling $\langle H_{12}^2 \rangle$ in (cm^{-1}) ²	characteristic ET time (ps)
D0	0.053 ± 0.002	3.40 ± 0.10	605.4 ± 183.0	101.1 ± 63.6
DA	0.045 ± 0.003	3.05 ± 0.13	927.3 ± 240.4	44.1 ± 23.1
P0	0.038 ± 0.002	3.33 ± 0.11	3571.8 ± 704.2	8.9 ± 3.3
PA	0.028 ± 0.003	2.26 ± 0.09	8928.1 ± 1413.4	2.0 ± 0.6

^aThe uncertainties are for 95% confidence intervals. The details for the calculation of the uncertainties are given in Supporting Information.

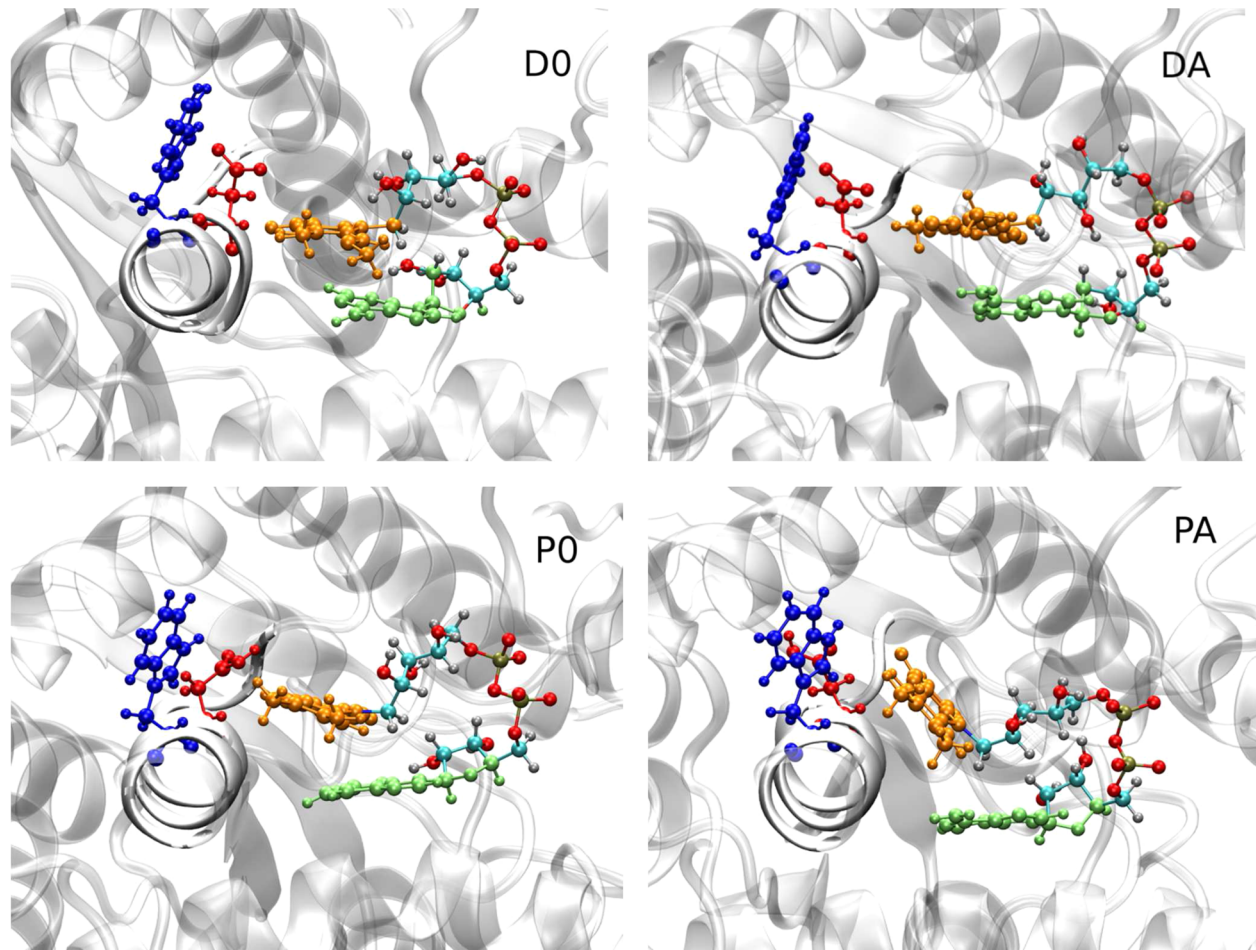


Figure 7. Differences in the conformation of the FAD cofactor in the photoactive center of AtCRY1 at the end of the 150 ns long simulations. Color code is the same as in Figure 1: D396 is shown in red, W400 in blue, ISO moiety of FAD in orange, and ADE moiety of FAD in light green.

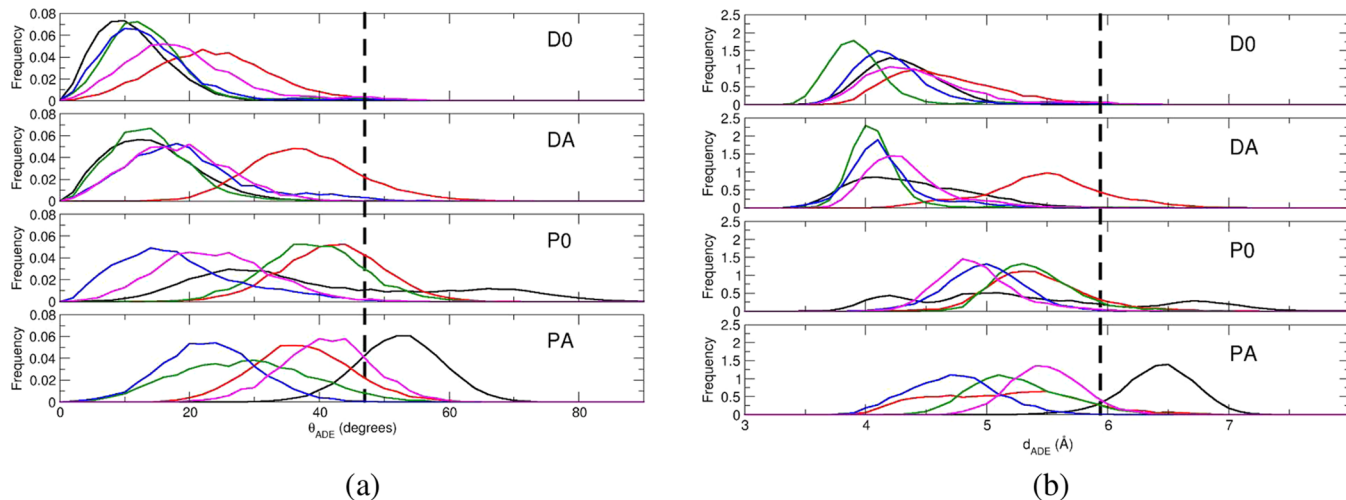


Figure 8. Relative orientations of ISO and ADE moieties of FAD. (a) Distribution of the angle θ_{ADE} between the mean planes of ADE and ISO. (b) Distribution of the distance d_{ADE} between the geometric center of the benzylic ring of ISO and the 6-membered ring of ADE. In both figures, the dashed black line is the value of the geometric parameter in the crystallographic structure (determined at pH 5.5, i.e., with protonated D396), and the color code is the same as in Figure 4

intermediate water molecules connect ISO-O4 or ISO-N5 with the carboxylate group of D396 via a network of hydrogen bonds. The deprotonated D396 is also most of the time involved in a hydrogen bond with the NH group of the indole ring. In deprotonated systems, the space that is freed by the conformational change of FAD can be filled with water molecules during the MD simulations. These water molecules can serve as bridges in the electron transfer pathways. We regrouped all the paths that passed through a water molecule (except those involving D396) in category C. The percentage of those pathways is around 25% in deprotonated systems (Table S5). All the other pathways are included in category D. These pathways involve nearby residues (e.g., G399 or F384) as bridges and are most often seen in D0 and DA systems. To conclude this analysis, we remark that for systems D0 and DA, the alternatives to the type A pathways are less efficient by almost 1 order of magnitude (Table S5), which accounts for the weaker electronic coupling within the deprotonated systems.

Marcus Electron Transfer Rates. The results of the preceding sections indicate that the rate of electron transfer between W400 and ISO* is (i) almost not thermally activated, and (ii) controlled by the fluctuation of the electronic coupling, which is higher when D396 is protonated and when ATP is bound to cryptochrome. In order to quantify the variation of the electron transfer rates between the various systems, we computed them in the framework of the Marcus theory, which requires estimates of the reorganization energy λ and of activation free energy ΔG^\ddagger . This can be done by construction of the free energy curves of each electronic state involved in the electron transfer, as detailed for example by Parson et al.⁵³ (technical details are given in the SI). Figure 2c shows the free energy of S1 and CT_{W400→ISO*} states as a function of the energetic gaps between these two electronic states in PA system (see also Figures S5 to S7). A quadratic fit leads to values of λ and ΔG^\ddagger that are presented in Table 4.

In agreement with the previous analysis, we note that the activation free energy for the W400 → ISO* ET is very small in every system (between 1 and 2 $k_B T$), so that the kinetics is mainly controlled by tunneling (see Table S6). The reorganization energies are rather large when compared to other ultrafast ET as in the photoreactive center or in DNA photolyases. Large λ

values would disfavor back ET. That said, the initial W400 → ISO* ET is followed by ps ET within the tryptophan triad so that the environment probably does not have time to relax and stabilize the initial CT state. Finally, the last column of Table 4 is the characteristic time for the ET process calculated as the inverse of the Marcus rate constant (eq 1), using H_{12} values obtained with the GMH scheme. The impact of the protonation state of D396 is clearly visible, the ET rates in PA and P0 systems being 1 order of magnitude greater than those in DA and D0 systems, respectively. ATP binding also seems to enhance the first electron transfer step but the effect is less pronounced than that of D396 protonation. These results are compared to experimental data and analyzed in more detail in the Discussion section.

Electron Transfer between ADE and ISO. Structure of the Photoactive Center. As mentioned previously, electron transfer from ADE may be an ISO* de-excitation pathway competing with the ET from W400. The enhancement of this pathway should lead to a decrease in the yield of ET along the triad of tryptophane residues and, consequently, also decrease in the yield of the metastable FAD°/FADH°. Interestingly, during our molecular dynamics simulations, we observed that the relative position of ADE with respect to ISO is strongly influenced by the protonation state of D396 and by ATP-binding. For illustration, Figure 7 shows the final configuration of the 150 ns-MD simulations for all 4 cases studied here.

When D396 is deprotonated, ADE and ISO cycles become nearly parallel and get closer (top panels in Figure 7). The angle between the two aromatic species increases in the P0 system (bottom-left panel) and is the biggest in the PA system (bottom-right panel). Figure 8 presents the distribution in the course of the MD simulations of two geometric measures which characterize the relative position of ADE and ISO: the angle θ_{ADE} formed by the planes of ISO and ADE, and the distance d_{ADE} separating the two moieties (defined as the distance between the geometric centers of the benzylic ring of ISO and the 6-membered ring of ADE). In the case of D0 systems, the two planes of ISO and ADE become nearly parallel in the course of the MD simulations (mean values of θ_{ADE} between 10° and 25°), whereas the initial value of this angle is around 47°. The situation

Table 5. Estimation of ADE → ISO* ET Rates from Marcus Parameters^a

system	activation free energy (eV)	reorganization energy (eV)	mean squared electronic coupling $\langle H_{12}^2 \rangle$ in (cm ⁻¹) ²	characteristic ET time (ps)
D0	0.092 ± 0.005	3.22 ± 0.13	56646.2 ± 5029.0	4.3 ± 1.0
DA	0.068 ± 0.004	4.25 ± 0.21	53570.7 ± 5426.5	2.1 ± 0.5
P0	0.093 ± 0.005	3.59 ± 0.14	38217.6 ± 4275.2	7.2 ± 1.9
PA	0.132 ± 0.007	2.35 ± 0.11	19699.3 ± 1894.0	49.7 ± 13.6

^aThe uncertainties are for 95% confidence intervals. The details for the calculation of the uncertainties are given in Supporting Information.

is similar for DA systems, even though slightly less pronounced. In the protonated systems (P0 and PA), the situation is less clear: each simulation leads to a different mean value. Nevertheless, on average, θ_{ADE} values are greater when D396 is protonated, and this effect is further amplified by ATP binding. The behavior of d_{ADE} is similar. In the deprotonated systems, the distance between the two cycles decreases from the crystallographic value (5.9 Å) to about 4–4.5 Å. When D396 is protonated, d_{ADE} usually lies between 4.5 and 5.5 Å. The bottom line is that most of the simulations of the D0 and DA systems yield π-stacked ISO and ADE, which should favor the nonproductive intramolecular ET within the FAD cofactor (ADE → ISO*) in these systems.

Rate of Electron Transfer from ADE to ISO*. We have used the same methods as for W400 → ISO* ET to estimate the rate of ET from ADE to ISO*. The CT_{ADE→ISO*} state lies typically above the CT_{W400→ISO*} state, which implies that the ET from ADE should be more activated than the ET from W400. Moreover, as can be seen in Figure 2b for the PA system, the probability to be in a conformation where the S1 state and the CT_{ADE→ISO*} state are degenerated is rather low. As for W400 → ISO* ET, the energetics aspects for this ET are similar for every protonation state of D396 and independent of ATP binding (see Table 2). Table 3 also gives the mean values of electronic coupling between S1 and CT_{ADE→ISO*} state as computed with the GMH scheme. As expected from the relative positions of ISO and ADE seen in the MD simulations, the electronic coupling is much greater in deprotonated systems: H_{12} values indeed follow a trend opposite to that observed for the W400 → ISO* ET. As a consequence, ADE → ISO* ET rates should increase when going from protonated to deprotonated systems.

Figure 2d shows the free energy profile for the ADE → ISO* ET reaction for PA system and Table 5 summarizes all Marcus parameters computed for the 4 systems. Activation free energies for the ADE → ISO* ET are slightly higher than for W400 → ISO* ET but the process remains weakly activated (the highest value of free energy is for system PA where it is as low as 5.3 $k_B T$). Overall, electron transfer is predicted to be faster from ADE than from W400 in deprotonated systems (D0 and DA). On the other hand, the ADE → ISO* ET rate is expected to be much slower than that for the W400 → ISO* ET when ATP is present and D396 is protonated.

Evaluation of D396 pK_a Shift. The results of the previous sections point toward an influence of ATP on the photo-reduction process via a modification of the protonation state of D396. To clarify how ATP may influence the pK_a of this amino acid residue, we estimated the shifts in pK_a of D396 in AtCRY1 with respect to an aspartic acid in aqueous phase. The values reported in Table 6 are the averages of pK_a shifts over snapshots extracted from the MD simulations every 500 ps. In each case, we observe a positive shift, indicating that pK_a of D396 in AtCRY1 is greater than the pK_a of an aspartic acid in water (3.86), which results from the fact that D396 is buried inside the hydrophobic protein. The values obtained from the structures extracted from deprotonated simulations (D0 and DA) are lower than those

Table 6. Evaluation of the Shift in D396 pK_a (ΔpK_a) from Continuum Electrostatic Calculations^a

system	ΔpK_a	ΔpK_a removing ATP
D0	0.73 (0.98)	—
DA	1.34 (1.14)	0.67 (1.10)
P0	3.80 (1.38)	—
PA	5.74 (1.30)	5.11 (1.27)

^aThe numbers in brackets are standard deviations.

obtained from protonated simulations (P0 and PA). This is due to the fact that equilibrium MD simulations favor structures corresponding to the protonation state in which they are performed. However, in each case, the pK_a shift is found to be greater when ATP is present than when it is absent (1.34 versus 0.73 for deprotonated simulations and 5.74 versus 3.80 for protonated simulations), revealing that ATP binding increases the pK_a of D396. The variation of pK_a may be due to direct electrostatic effects of ATP, but also to an indirect effect through structural modifications of the protein. In order to estimate the electrostatic effect of ATP, we used structures from DA and PA simulations and performed pK_a shifts evaluations removing the ATP molecule (see the last column of Table 6). In the two cases, the pK_a shift decreases by approximately 0.6. This indicates that ATP binding has a direct electrostatic effect that favors protonation of D396. However, in the case of PA, the pK_a shift when ATP molecule is removed is still greater than the one found with structures extracted from P0 simulations. This shows that there is also an indirect (structural) role of ATP favoring D396 protonation. Overall, those results indicate that ATP binding indeed does increase the pK_a of D396, in agreement with experimental data.

DISCUSSION

This study is the first theoretical attempt to explain the striking effects of ATP binding and of the protonation state of the aspartic acid in the vicinity of the FAD chromophore on its photo-reduction in plant cryptochromes. In the following, we will discuss our results in the context of published experimental evidence and theoretical predictions.

In 2007, Immeln et al. showed that ATP binding dramatically slows down the reoxidation of FADH^o in the light-sensitive domain of *Chlamydomonas* cryptochrome.²⁵ Similar effects of ATP were observed for full-length AtCRY1. Burney et al.²⁴ also reported an increased resistance of AtCRY1 to denaturation by guanidine and to proteolysis by trypsin in the presence of ATP. These effects were attributed to a conformational rearrangement of AtCRY1 upon ATP binding. Since the previously published crystal structures of AtCRY1 PHR domain¹⁰ with and without ATP are virtually identical, Burney et al. argued that the proposed conformational change may involve the C-terminal domain of cryptochrome. Direct evidence of such a conformational change is, however, still missing. Very recently, Müller and collaborators³³ further investigated the effects of ATP binding on the

photoreduction of FAD_{ox} in *AtCRY1-PHR*. They found that ATP not only substantially enhances the yield of the photo-induced transients but also changes the kinetics of their formation and decay, indicating an ATP-induced change of the photoreduction mechanism. They also reported that in the absence of ATP, the yield of FAD_{ox} photoreduction substantially drops when increasing pH within a physiologically relevant pH interval between 7 and 8. This, however, is no longer the case when ATP is present: the transient absorption traces reflecting the evolution of the transients' concentrations within the first 10 μ s are virtually constant up to pH \sim 9. To interpret the increased yield of FAD_{ox} photoreduction to FADH[°] and the lack of response to pH changes within the studied pH interval, Müller et al. proposed that ATP binding modifies the pK_a of D396 from \sim 7.4 to >9 . Our estimate of pK_a shifts upon ATP binding support this hypothesis, showing ATP binding effectively increases the pK_a of D396 (although, as stated in the methods section, a direct quantitative comparison of our values with the experimental values is not possible). However, the change of pK_a might not fully explain the change in mechanism: while in the absence of ATP, a significant fraction of FADH[°]-Trp[°] radical pairs seemed to be formed in an ultrafast manner (consistent with the ultrafast proton transfer from D396(H) and the subsequent ultrafast W400(H)⁺ deprotonation by D396⁻, as suggested by Solov'yov et al.²⁸), the 200 ns phase reflecting TrpH^{°+} deprotonation and the 1.5 μ s phase reflecting slow FAD^{°-} protonation²² are much more pronounced in the signals recorded in the presence of ATP.³³

In this work, we have explored the impact of the protonation state of D396 and that of ATP binding on the structure of the photoactive center by means of computer simulations. Our data indicate that protonated systems (P0 and PA) display structures in which ISO remains in close contact to W400, like in the crystallographic structure, especially when ATP is bound to cryptochrome. When D396 is deprotonated (D0 and DA), the distance between W400 and ISO increases and the FAD cofactor adopts conformations very different from the crystallographic structure. According to our calculations, the kinetics of the first ET step in *AtCRY1*, i.e., ET from W400 to ISO*, is much faster (one to two orders of magnitude) in the systems PA and P0 than in the systems DA and D0. These rate differences result essentially from differences in electronic coupling strengths among the four systems (see Table 3), in direct connection to the variations of the ISO-W400 distances. The analysis of the tunneling pathways further indicate that in the systems PA and P0, thanks to the close contact between the electron donor and acceptor, the abstracted electron can jump directly from W400 to ISO without molecular intermediates. On the contrary, several types of tunneling pathways are encountered in systems DA and D0, running either through D396, G399 or F384 or through water molecules, and all these pathways are less efficient than those common in the systems P0 and PA. A diminution of the ET rate from W400, predicted for example for system D0, would open the door for competitive relaxation pathways: the slower the first electron transfer, the higher the probability of a nonproductive relaxation of ISO*. This would explain why the yield of photoreduction without ATP is lower at high pH (system D0), than at low pH (system P0), as observed by Müller and collaborators.³³ In the presence of ATP (system PA), the yield stays high even at higher pH, up to pH \sim 9. Note that we will not discuss the DA system any further as its existence would require a relatively high pH (well above 9), and should hence not be physiologically relevant.

Out of the plausible competing ISO* quenching pathways (see Introduction), we have closely analyzed the possible electron transfer from the adenine moiety of FAD, which is the most obvious candidate for competitive ET. The occurrence of this ET should vary significantly depending on the structure of the photoactive center, which is not expected, for example for internal conversions, as the energetics of the excited states are only marginally affected by protonation of D396 or ATP binding (see Table 2). Indeed, we have shown that while in the presence of ATP and at low pH, the W400 \rightarrow ISO* ET is faster than the ADE \rightarrow ISO* ET, in the absence of ATP and at low pH (P0), the rates of the two ETs should be of similar magnitude. The intramolecular quenching by ET from ADE becomes more important at the expense of the W400 \rightarrow ISO* ET, which is the initial step preceding charge migration along the triad of tryptophane residues. This would result in a lower yield of FAD^{°-}/FADH[°], consistent with the experimental findings of Müller et al. Note that also in the ultrafast study of Immeln et al. (conducted apparently in the absence of ATP), up to \sim 40% of excited flavins were estimated to relax along pathways other than ET from the nearest Trp residue in *Chlamydomonas* CPH1.²⁵ At high pH and with no ATP bound, the ET ADE \rightarrow ISO* becomes dominant, essentially blocking the productive ET from W400. This is, again, coherent with the experimentally observed decrease of FAD^{°-}/FADH[°] yield with increasing pH in the absence of ATP.³³

Overall, our data strongly suggest that the ATP-dependence of the yield of FAD^{°-}/FADH[°] observed experimentally finds its origin in the modulations of the branching ratio among the FAD* relaxation pathways. ATP binding and protonation of D396 thus lead to conformations of the photoactive site that are ideally suited for fast ET from W400. Given the time range accessible to MD simulations (few hundreds of nanoseconds), we cannot rule out that ATP induces large-scale conformational changes in the protein including the C-terminal domain (as suggested by Burney et al.²⁴), as these would probably occur on a much slower time scale. On the other hand, the results of Müller et al. covering the nanosecond to millisecond time scales did not reveal any significant difference in the photochemistry of *AtCRY1-PHR* and the full-length *AtCRY1*, suggesting that large conformational changes are not required to account for the effect of ATP on the primary photoreaction steps.³³ Actually, as explained above, our computational results show that the experimental trend can be interpreted without the need to invoke large-scale conformational changes. Also, our results are in no contradiction with the similarity observed between the two crystallographic structures with and without ATP. Indeed, both structures have been obtained at a pH of 5.5,¹⁰ at which, based on the conclusions of Müller et al., D396 is very likely to be protonated even in the absence of ATP. The conformations of FAD and its close environment in the corresponding P0 and PA systems at the end of our long (150 ns) simulations do not deviate much from those in the crystallographic structures.

On the basis of classical molecular dynamics simulations, Solov'yov et al. proposed that the electron transfer from W400 to ISO* in cryptochrome is directly followed by an ultrafast proton transfer from D396 to FAD^{°-}, before electron transfer can occur within the tryptophan triad.²⁸ The argument in favor of this mechanism is the observation of a fast reorientation of the side chain of D396 in MD simulations of the {W400^{°+}, ISO^{°-}} state. This reorientation leads to a conformation in which the acidic proton of D396 is well positioned to be transferred to flavin. Müller et al. showed that even though it is never prevailing, this

mechanism is indeed possible and is more important when ATP is absent. The estimated ratio between the “through tryptophan triad” ET mechanism and the “ultrafast proton transfer” mechanism changes from 2:1 in the absence of ATP to 7:1 in its presence. In our MD simulations, we observed fundamentally different behaviors of the P0 and the PA systems with respect to the orientation of the D396 side chain. In P0, a hydrogen bond is formed between D396 and ISO for ~70% of the simulation time. In PA, however, this is almost never the case (see Figure 6) and the COOH of D396 remains H-bonded to the carbonyl oxygen of M381 most of the time. This difference in the P0 and PA hydrogen bonding patterns could explain the increased proportion of the “ultrafast proton transfer” mechanism observed in absence of ATP, since the acidic proton of D396 is already well positioned to be transferred to flavin before the ET transfer from W400 to ISO* takes place. However, care must be taken with such conclusions since the right orientation of the carboxyl group of D396 is a necessary but not sufficient condition for the transfer to happen. The activation barrier for transferring the proton is another key parameter determining the likelihood of a proton transfer event.

CONCLUSION

Recent experimental study³³ revealed that the mechanism of FAD_{ox} photoreduction in *Arabidopsis* CRY1 depends on whether or not ATP is bound to the protein, and it was shown that the yield of the semireduced flavin FAD^{°-}/FADH[°] drops dramatically with increasing pH, but only in the absence of ATP. The central goal of the present theoretical study was to understand the molecular origins of these findings. Since these pronounced effects are most likely connected to the protonation state and flexibility of D396, the putative proton donor to FAD^{°-}, we have investigated, how ATP binding and the protonation state of D396 affect the photoactive center of the protein (i.e., the FAD cofactor and the amino acids in its immediate vicinity).

Our results suggest that deprotonation of D396 induces a substantial change in the conformation of the FAD cofactor, the FAD isoalloxazine ring moving closer to the FAD adenine ring (to form a π -stacked complex) and farther from W400. Deprotonation of D396 thus indirectly hampers a productive electron transfer from W400 to the ISO* moiety and favors an ISO* self-quenching by intramolecular ET from adenine to isoalloxazine. In contrast, protonation of D396 reduces the electronic coupling for ET from ADE and enhances that of the W400 \rightarrow ISO* ET, which makes the corresponding productive ET more likely and hence faster. ATP binding to a cryptochromes with protonated D396 brings ISO and W400 even closer together. Together with the postulated³³ ATP-induced increase in the pK_a of D396, these results explain how ATP enhances the yield of flavin photoreduction and why the yield of this reaction diminishes so strongly with increasing basicity in the absence of ATP. The computational results presented in this work should stimulate experimental studies aimed at direct determination of the rates of the ultrafast W400 \rightarrow ISO* ET as a function of pH and ATP binding in plant cryptochromes.

ASSOCIATED CONTENT

Supporting Information

Computational details including force field parameters for nonstandard molecular fragments, assessment of various exchange-correlation functionals for TD-DFT calculations; methodology for constructing Marcus-like free energy curves

and for the evaluation of statistical uncertainties; computational data that were not included in the text. This material is available free of charge via the Internet at <http://pubs.acs.org>.

AUTHOR INFORMATION

Corresponding Authors

fabien.cailliez@u-psud.fr
aurelien.de-la-lande@u-psud.fr

Notes

The authors declare no competing financial interest.

ACKNOWLEDGMENTS

We acknowledge the WESTGRID (Canada) network for providing us with substantial computational resources. This work was performed using HPC resources from GENCI [CCRT/CINES/IDRIS] (Grant 2013-2014, Project Number c2014076913). We are grateful to Klaus Brettel and Jean-Pierre Bouly for fruitful discussions. We also appreciated the help of Bernard Lévy, Pascal Pernot and Julien Toulouse. P.M. acknowledges the support by the French Agence Nationale de la Recherche (Grant #ANR-12-BSV8-0001-01).

REFERENCES

- (1) Ahmad, M.; Cashmore, A. R. *Nature* **1993**, *366*, 162–166.
- (2) Cashmore, A. R.; Jarillo, J. A.; Wu, Y. J.; Liu, D. *Science* **1999**, *284*, 760–765.
- (3) Chaves, I.; Pokorny, R.; Byrdin, M.; Hoang, N.; Ritz, T.; Brettel, K.; Essen, L.-O.; van der Horst, G. T. J.; Batschauer, A.; Ahmad, M. *Annu. Rev. Plant Biol.* **2011**, *62*, 335–364.
- (4) van der Horst, G. T. J.; Muijters, M.; Kobayashi, K.; Takano, R.; Kanno, S.; Takao, M.; de Wit, J.; Verkerk, A.; Eker, A. P.; van Leenen, D.; Buijs, R.; Bootsma, D.; Hoeijmakers, J. H.; Yasui, A. *Nature* **1999**, *398*, 627–630.
- (5) Mouritsen, H.; Janssen-Bienhold, U.; Liedvogel, M.; Feenders, G.; Stalleicken, J.; Dirks, P.; Weiler, R. *Proc. Natl. Acad. Sci. U. S. A.* **2004**, *101*, 14294–14299.
- (6) Möller, A.; Sagasser, S.; Wiltschko, W.; Schierwater, B. *Naturwissenschaften* **2004**, *91*, 585–588.
- (7) Ritz, T.; Adem, S.; Schulten, K. *Biophys. J.* **2000**, *78*, 707–718.
- (8) Maeda, K.; Robinson, A. J.; Henbest, K. B.; Hogben, H. J.; Biskup, T.; Ahmad, M.; Schleicher, E.; Weber, S.; Timmel, C. R.; Hore, P. J. *Proc. Natl. Acad. Sci. U. S. A.* **2012**, *109*, 4774–4779.
- (9) Selby, C. P.; Sancar, A. *Proc. Natl. Acad. Sci. U. S. A.* **2006**, *103*, 17696–17700.
- (10) Brautigam, C. A.; Smith, B. S. *Proc. Natl. Acad. Sci. U. S. A.* **2004**, *101*, 12142–12147.
- (11) Czarna, A.; Berndt, A.; Singh, H. R.; Grudziecki, A.; Ladurner, A. G.; Timinszky, G.; Kramer, A.; Wolf, E. *Cell* **2013**, *153*, 1394–1405.
- (12) Xing, W.; Busino, L.; Hinds, T. R.; Marionni, S. T.; Saifee, N. H.; Bush, M. F.; Pagano, M.; Zheng, N. *Nature* **2013**, *496*, 64–68.
- (13) Levy, C.; Zoltowski, B. D.; Jones, A. R.; Vaidya, A. T.; Top, D.; Widom, J.; Young, M. W.; Scrutton, N. S.; Crane, B. R.; Leys, D. *Nature* **2013**, *495*, E3–E4.
- (14) Partch, C. L.; Clarkson, M. W.; Ozgür, S.; Lee, A. L.; Sancar, A. *Biochemistry* **2005**, *44*, 3795–3805.
- (15) Lukacs, A.; Eker, A. P. M.; Byrdin, M.; Brettel, K.; Vos, M. H. *J. Am. Chem. Soc.* **2008**, *130*, 14394–14395.
- (16) Brettel, K.; Byrdin, M. *Curr. Opin. Struct. Biol.* **2010**, *20*, 693–701.
- (17) Biskup, T.; Paulus, B.; Okafuji, A.; Hitomi, K.; Getzoff, E. D.; Weber, S.; Schleicher, E. *J. Biol. Chem.* **2013**, *288*, 9249–9260.
- (18) Krapf, S.; Weber, S.; Koslowski, T. *Phys. Chem. Chem. Phys.* **2012**, *14*, 11518–11524.
- (19) Kholmurodov, K.; Dushanov, E.; Yasuoka, K. *Adv. Biosci. Biotechnol.* **2012**, *3*, 169–180.
- (20) Woiczikowski, P. B.; Steinbrecher, T.; Kubáč, T.; Elstner, M. *J. Phys. Chem. B* **2011**, *115*, 9846–9863.

- (21) Cheung, M. S.; Daizadeh, I.; Stuchebrukhov, A. A.; Heelis, P. F. *Biophys. J.* **1999**, *76*, 1241–1249.
- (22) Langenbacher, T.; Immeln, D.; Dick, B.; Kottke, T. *J. Am. Chem. Soc.* **2009**, *131*, 1427–14280.
- (23) Iwata, T.; Zhang, Y.; Hitomi, K.; Getzoff, E. D.; Kandori, H. *Biochemistry* **2010**, *49*, 8882–8891.
- (24) Burney, S.; Hoang, N.; Caruso, M.; Dudkin, E. A.; Ahmad, M.; Bouly, J.-P. *FEBS Lett.* **2009**, *583*, 1427–1433.
- (25) Immeln, D.; Weigel, A.; Kottke, T.; Pérez Lustres, J.-L. *J. Am. Chem. Soc.* **2012**, *134*, 12536–12546.
- (26) Liu, Z.; Zhang, M.; Guo, X.; Tan, C.; Li, J.; Wang, L.; Sancar, A.; Zhong, D. *Proc. Natl. Acad. Sci. U. S. A.* **2013**, *110*, 12972–12977.
- (27) Biskup, T.; Hitomi, K.; Getzoff, E. D.; Krapf, S.; Koslowski, T.; Schleicher, E.; Weber, S. *Angew. Chem., Int. Ed.* **2011**, *50*, 12647–12651.
- (28) Solov'yov, I. A.; Domratcheva, T.; Shahi, A. R. M.; Schulten, K. J. *Am. Chem. Soc.* **2012**, *134*, 18046–18052.
- (29) Solov'yov, I. A.; Domratcheva, T.; Schulten, K. *Sci. Rep.* **2014**, *4*, 3845.
- (30) Bouly, J.-P.; Giovani, B.; Djamei, A.; Mueller, M.; Zeugner, A.; Dudkin, E. A.; Batschauer, A.; Ahmad, M. *Eur. J. Biochem.* **2003**, *270*, 2921–2928.
- (31) Immeln, D.; Schlesinger, R.; Heberle, J.; Kottke, T. *J. Biol. Chem.* **2007**, *282*, 21720–21728.
- (32) Giovani, B.; Byrdin, M.; Ahmad, M.; Brettel, K. *Nat. Struct. Mol. Biol.* **2003**, *10*, 489–490.
- (33) Müller, P.; Bouly, J.-P.; Hitomi, K.; Balland, V.; Getzoff, E. D.; Ritz, T.; Brettel, K. *Sci. Rep.* **2014**, *4*, 5175.
- (34) Exner, V.; Alexandre, C.; Rosenfeldt, G.; Alfarano, P.; Nater, M.; Caflisch, A.; Gruisse, W.; Batschauer, A.; Hennig, L. *Plant Physiol.* **2010**, *154*, 1633–1645.
- (35) Gauden, M.; Yeremenko, S.; Laan, W. *Biochemistry* **2005**, *44*, 3653–3662.
- (36) Kennis, J. T. M.; Crosson, S.; Gauden, M.; van Stokkum, I. H. M.; Moffat, K.; van Grondelle, R. *Biochemistry* **2003**, *42*, 3385–3392.
- (37) Holzer, W.; Penzkofer, A.; Fuhrmann, M.; Hegemann, P. *Photochem. Photobiol.* **2002**, *75*, 479–487.
- (38) Heelis, P. F. *Chem. Soc. Rev.* **1982**, *11*, 15–39.
- (39) Berman, H. M.; Westbrook, J.; Feng, Z.; Gilliland, G.; Bhat, T. N.; Weissig, H.; Shindyalov, I. N.; Bourne, P. E. *Nucleic Acids Res.* **2000**, *28*, 235–242, <http://www.rcsb.org/>.
- (40) Jorgensen, W. L.; Chandrasekhar, J.; Madura, J. D.; Impey, R. W.; Klein, M. L. *J. Chem. Phys.* **1983**, *79*, 926–935.
- (41) MacKerell, A. D., Jr.; Feig, M.; Brooks, C. L., III. *J. Comput. Chem.* **2004**, *25*, 1400–1415.
- (42) Phillips, J. C.; Braun, R.; Wang, W.; Gumbart, J.; Tajkhorshid, E.; Villa, E.; Chipot, C.; Skeel, R. D.; Kalé, L.; Schulten, K. *J. Comput. Chem.* **2005**, *26*, 1781–1802.
- (43) Ryckaert, J.-P.; Ciccotti, G.; Berendsen, H. J. C. *J. Comput. Phys.* **1977**, *23*, 327–341.
- (44) Martyna, G. J.; Tobias, D. J.; Klein, M. L. *J. Chem. Phys.* **1994**, *101*, 4177–4189.
- (45) Feller, S. E.; Zhang, Y.; Pastor, R. W.; Brooks, B. R. *J. Chem. Phys.* **1995**, *103*, 4613–4621.
- (46) Yu, H.; Ratheal, I.; Artigas, P.; Roux, B. *Nat. Struct. Mol. Biol.* **2011**, *18*, 1159–1163.
- (47) Brooks, R. R.; Brooks, C. L., III; Mackerell, A. D., Jr.; Nilsson, L.; Petrella, R. J.; Roux, B.; Won, Y.; Archontis, G.; Bartels, C.; Boresch, S.; Caflisch, A.; Caves, L.; Cui, Q.; Dinner, A. R.; Feig, M.; Fischer, S.; Gao, J.; Hodoscek, M.; Im, W.; Kuczera, K.; Lazaridis, T.; Ma, J.; Ovchinnikov, V.; Paci, E.; Pastor, R. W.; Post, C. B.; Pu, J. Z.; Schaefer, M.; Tidor, B.; Venable, R. M.; Woodcock, H. L.; Wu, X.; Yang, W.; York, D. M.; Karplus, M. *J. Comput. Chem.* **2009**, *30*, 1545–1614.
- (48) (a) Nina, M.; Beglov, D.; Roux, B. *J. Phys. Chem. B* **1997**, *101*, 5239–5248. (b) Banavali, N. K.; Roux, B. *J. Phys. Chem. B* **2002**, *106*, 11026–11035.
- (49) Tachiya, M. *J. Phys. Chem.* **1989**, *93*, 7050–7052.
- (50) Tully, J. C. *J. Chem. Phys.* **1990**, *93*, 1061–1071.
- (51) Hack, M. D.; Truhlar, D. G. *J. Chem. Phys.* **2001**, *114*, 9305–9314.
- (52) Kubař, T.; Elstner, M. *J. Phys. Chem. B* **2010**, *114*, 11221–11240.
- (53) Parson, W. W.; Chu, Z. T.; Warshel, A. *Biophys. J.* **1998**, *74*, 182–191.
- (54) Casida, M. E. Time-dependent density-functional response theory for molecules. In *Recent Advances in Density Functional Methods, Part I*; Chong, D.P., Ed.; World Scientific: Singapore, 1995; p 155.
- (55) Frisch, M. J.; Trucks, G. W.; Schlegel, H. B.; Scuseria, G. E.; Robb, M. A.; Cheeseman, J. R.; Scalmani, G.; Barone, V.; Mennucci, B.; Petersson, G. A.; Nakatsuji, H.; Caricato, M.; Li, X.; Hratchian, H. P.; Izmaylov, A. F.; Bloino, J.; Zheng, G.; Sonnenberg, J. L.; Hada, M.; Ehara, M.; Toyota, K.; Fukuda, R.; Hasegawa, J.; Ishida, M.; Nakajima, T.; Honda, Y.; Kitao, O.; Nakai, H.; Vreven, T.; Montgomery, J. A., Jr.; Peralta, J. E.; Ogliaro, F.; Bearpark, M.; Heyd, J. J.; Brothers, E.; Kudin, K. N.; Staroverov, V. N.; Kobayashi, R.; Normand, J.; Ragahavachari, K.; Rendell, A.; Burant, J. C.; Iyengar, S. S.; Tomasi, J.; Cossi, M.; Rega, N.; Millam, N. J.; Klene, M.; Knox, J. E.; Cross, J. B.; Bakken, V.; Adamo, C.; Jaraillo, J.; Gomperts, R.; Stratmann, R. E.; Yazev, O.; Austin, A. J.; Cammi, R.; Pomelli, C.; Ochterski, J. W.; Martin, R. L.; Morokuma, K.; Zakrzewski, V. G.; Voth, G. A.; Salvador, P.; Dannenberg, J. J.; Dapprich, S.; Daniels, A. D.; Farkas, Ö.; Foresman, J. B.; Ortiz, J. V.; Cioslowski, J.; Fox, D. J. *Gaussian 09*, Revision D.01; Gaussian, Inc.: Wallingford, CT, 2009.
- (56) Godbout, N.; Salahub, D. R.; Andzelm, J.; Wimmer, E. *Can. J. Chem.* **1992**, *70*, 560–571.
- (57) Singh, U. C.; Kollman, P. A. *J. Comput. Chem.* **1986**, *7*, 718–730.
- (58) Field, M. J.; Bash, P. A.; Karplus, M. *J. Comput. Chem.* **1990**, *11*, 700–733.
- (59) Dreuw, A.; Weisman, J. L.; Head-Gordon, M. *J. Chem. Phys.* **2003**, *119*, 2943–2946.
- (60) Jacquemin, D.; Perpète, E. A.; Ciofini, I.; Adamo, C.; Valero, R.; Zhao, Y.; Truhlar, D. G. *J. Chem. Theory Comput.* **2010**, *6*, 2071–2085.
- (61) Peverati, R.; Tuhr, D. G. *Phys. Chem. Chem. Phys.* **2012**, *14*, 11363–11370.
- (62) Sini, G.; Sears, J. S.; Brédas, J.-L. *J. Chem. Theory Comput.* **2011**, *7*, 702–709.
- (63) Yanai, T.; Tew, D. P.; Handy, N. C. *Chem. Phys. Lett.* **2004**, *393*, 51–57.
- (64) Peverati, R.; Truhlar, D. G. *J. Phys. Chem. Lett.* **2011**, *2*, 2810–2817.
- (65) Chai, J.-D.; Head-Gordon, M. *Phys. Chem. Chem. Phys.* **2008**, *10*, 6615–6620.
- (66) Cave, R.; Newton, M. D. *J. Chem. Phys.* **1997**, *106*, 9213–9226.
- (67) Beratan, D. N.; Onuchic, J. N.; Hopfield, J. J. *J. Chem. Phys.* **1987**, *86*, 4488–4498.
- (68) Beratan, D. N.; Betts, J. N.; Onuchic, J. N. *Science* **1991**, *252*, 1285–1288.
- (69) Dijkstra, E. W. *Numer. Math.* **1959**, *1*, 269–271.
- (70) de la Lande, A.; Babcock, N.; Řezáč, J.; Sanders, B. C.; Salahub, D. R. *Proc. Natl. Acad. Sci. U. S. A.* **2010**, *107*, 11799–11804.
- (71) El Hammi, E.; Houée-Lévin, C.; Řezáč, J.; Lévy, B.; Demachy, I.; Baciou, L.; de la Lande, A. *Phys. Chem. Chem. Phys.* **2012**, *14*, 13872–13880.
- (72) Liang, H.-X.; Nocek, J. M.; Huang, K.; Hayes, R. T.; Kurnikov, I. V.; Beratan, D. N.; Hoffman, B. J. *Am. Chem. Soc.* **2002**, *124*, 65849–6859. (b) Keinan, S.; Nocek, J. M.; Hoffman, B. J.; Beratan, D. N. *Phys. Chem. Chem. Phys.* **2012**, *14*, 13881–13889. (c) Lin, J.; Balabin, I. A.; Beratan, D. N. *Science* **2005**, *310*, 311–313.
- (73) Balabin, I. A.; Beratan, D. N.; Skourtis, S. S. *Phys. Rev. Lett.* **2008**, *101*, 158102–4.
- (74) Balabin, I. A.; Onuchic, J. N. *Science* **2000**, *290*, 114–117.